

# Cytochrome *c* causes pore formation in cardiolipin-containing membranes

Chris L. Bergstrom<sup>a</sup>, Paul A. Beales<sup>b,1</sup>, Yang Lv<sup>a</sup>, T. Kyle Vanderlick<sup>b,2</sup>, and John T. Groves<sup>a,2</sup>

<sup>a</sup>Department of Chemistry, Princeton University, Princeton, NJ 08544; and <sup>b</sup>Department of Chemical and Environmental Engineering, Yale University, New Haven, CT 06520

Contributed by John T. Groves, March 1, 2013 (sent for review September 11, 2012)

The release of cytochrome *c* from mitochondria is a key signaling mechanism in apoptosis. Although extramitochondrial proteins are thought to initiate this release, the exact mechanisms remain unclear. Cytochrome *c* (cyt *c*) binds to and penetrates lipid structures containing the inner mitochondrial membrane lipid cardiolipin (CL), leading to protein conformational changes and increased peroxidase activity. We describe here a direct visualization of a fluorescent cyt *c* crossing synthetic, CL-containing membranes in the absence of other proteins. We observed strong binding of cyt *c* to CL in phospholipid vesicles and bursts of cyt *c* leakage across the membrane. Passive fluorescent markers such as carboxyfluorescein and a 10-kDa dextran polymer crossed the membrane simultaneously with cyt *c*, although larger dextrans did not. The data show that these bursts result from the opening of lipid pores formed by the cyt *c*-CL conjugate. Pore formation and cyt *c* leakage were significantly reduced in the presence of ATP. We suggest a model, consistent with these findings, in which the formation of toroidal lipid pores is driven by initial cyt *c*-induced negative spontaneous membrane curvature and subsequent protein unfolding interactions. Our results suggest that the CL-cyt *c* interaction may be sufficient to allow cyt *c* permeation of mitochondrial membranes and that cyt *c* may contribute to its own escape from mitochondria during apoptosis.

electrostatic | GUV | permeability | flux | cholesterol

Cytochrome *c* (cyt *c*) is a mitochondrial electron transfer protein localized to the inner mitochondrial membrane of nonapoptotic cells by strong electrostatic and hydrophobic interactions with cardiolipin (CL) (1–6). This negatively charged lipid, which comprises ~10 mol% of the inner mitochondrial membrane (7), and its oxidation products, play a central role in apoptotic signaling (8, 9). Release of cyt *c* from mitochondria induces apoptosis. An initial step in this process involves changes in the cyt *c*-CL interaction that anchors the protein to the inner membrane. Attendant protein conformational changes and hydrophobic interactions with the lipid confer catalytic activities to the cyt *c*-CL complex (1, 4, 9–12), which causes CL oxidation. Signaling at this stage may also involve cyt *c* tyrosine phosphorylation (13, 14) and the balance of mitochondrial ATP (15). Subsequently, cyt *c* exits the mitochondria via outer membrane permeabilization (2). Although the exact mechanism of this permeabilization remains unclear (2), it is thought to be orchestrated by the proapoptotic Bcl-2 family of proteins including Bid, Bax, and Bak, which can act cooperatively to form pores in the outer membrane (16–21).

Cyt *c* causes structural changes to CL-containing membranes, including penetration into liposome interiors and transition to an inverted hexagonal ( $H_{II}$ ) phase—a cylindrical lipid structure with head groups lining an aqueous interior (6, 22, 23). Recently, cyt *c*-derived peptides were observed to cross plasma membranes (24). Under apoptotic conditions, outer mitochondrial membranes were found to contain ~40 mol% CL due to migration of this lipid from the inner membrane (9). Taken together, these results suggest that the cyt *c*-CL interaction may lead to structural changes in the outer membrane and thereby contribute to the escape of cyt *c* from mitochondria during apoptosis.

Single-giant unilamellar vesicle (GUV) microscopy has emerged recently as a powerful technique to investigate membrane leakage and pore formation induced by proteins and peptides (25–28). These experiments are similar in concept to black lipid membrane conductance experiments, except instead of measuring the flow of small ions across a membrane, the passage of large macromolecules can be directly observed by fluorescence. The goal of this study was to examine the intrinsic behavior of cyt *c* in contact with CL-containing GUV model membranes. We labeled these GUVs as well as yeast cyt *c* with fluorophores and directly observed the passage of this protein as well as passive fluorescent dextran polymers across the GUV membrane bilayer using confocal microscopy. The results show that discrete pores were formed in the membrane, allowing rapid transmembrane leakage of cyt *c* as a result of the cyt *c*-CL interaction.

## Results

In the most basic experiment, we assembled mixed populations of giant 1,2-dioleoyl-*sn*-glycero-3-phosphocholine (DOPC) vesicles, some containing CL and some without, in a medium containing fluorescently labeled cyt *c*. Using confocal microscopy, we observed strong binding of cyt *c* with CL-containing membranes (red halo) and almost no cyt *c* association with membranes lacking CL (blue halo) (Fig. 1A). We also observed that cyt *c* was able to penetrate the CL-containing vesicles and fill the interior volume (vesicle 2), whereas the DOPC-only vesicles were robust under these conditions (vesicle 1).

To illuminate the mechanism of cyt *c* transport across the GUV membranes, a fluorescent neutrally charged dextran was incubated with the vesicles. Before the addition of cyt *c*, the vesicles were not leaky to a 10-kDa dextran (Fig. S1, *SI Text*); after cyt *c* was added, there was a lag time, and then both cyt *c* and the similarly sized 10-kDa dextran were observed to enter the interior of each vesicle rapidly and simultaneously (Fig. 1C–E). The relative interior brightness of GUVs is depicted by the bar graphs (Fig. 1) or histograms (Fig. S2, *SI Text*). By contrast, a 70-kDa dextran (Fig. 1B, green channel) was largely excluded from the GUV interior, even though cyt *c* had entered the vesicle interiors (red channel), indicating an apparent size limit for membrane permeation.

To investigate the kinetics of this permeabilizing effect by cyt *c*, we collected confocal time-lapse images of the leakage of cyt *c* and 10-kDa dextran into individual vesicles. In these experiments, fluorescent cyt *c* diffused into the visual field from its site of addition (Fig. S3, *SI Text*)—this method ensured our ability to monitor GUVs before the onset of leakage and to record leakage

Author contributions: C.L.B., P.A.B., Y.L., T.K.V., and J.T.G. designed research; C.L.B., P.A.B., and Y.L. performed experiments; C.L.B., P.A.B., Y.L., T.K.V., and J.T.G. analyzed data; and C.L.B., P.A.B., and J.T.G. wrote the paper.

The authors declare no conflict of interest.

<sup>1</sup>Present address: Centre for Molecular Nanoscience, School of Chemistry, University of Leeds, Leeds LS2 9JT, United Kingdom.

<sup>2</sup>To whom correspondence may be addressed. E-mail: jtgroves@princeton.edu or kyle.vanderlick@yale.edu.

This article contains supporting information online at [www.pnas.org/lookup/suppl/doi:10.1073/pnas.1303819110/-DCSupplemental](http://www.pnas.org/lookup/suppl/doi:10.1073/pnas.1303819110/-DCSupplemental).

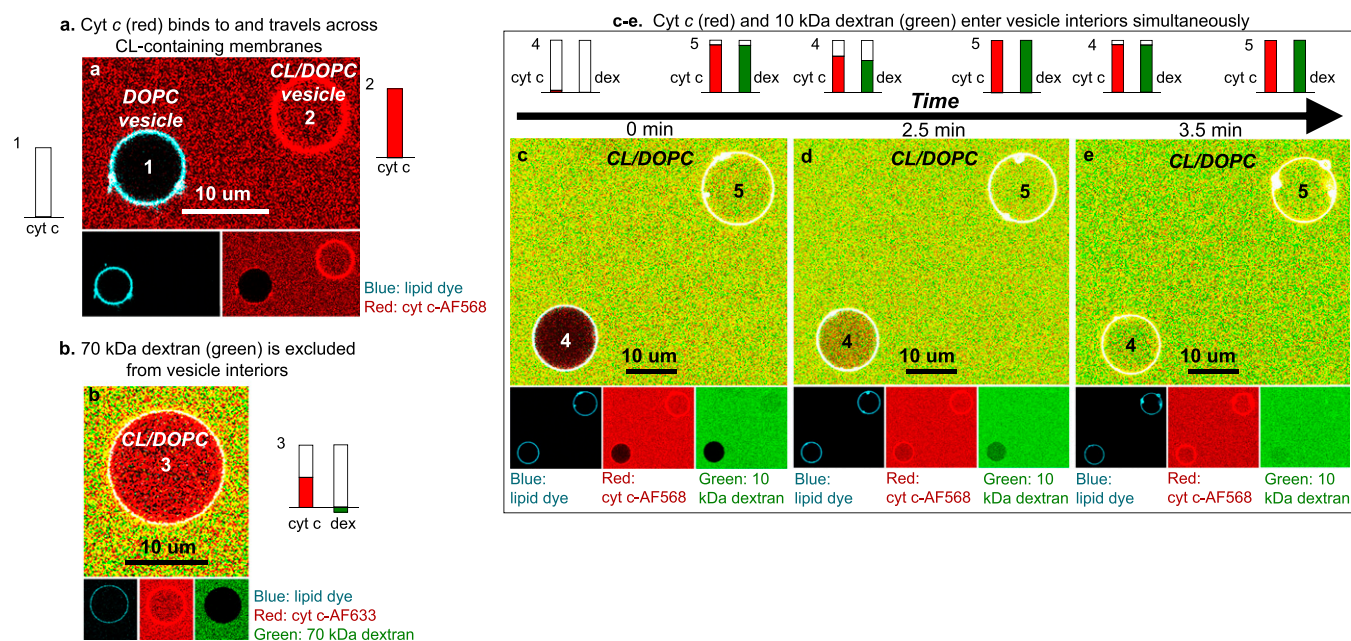


**Fig. 1.** Cyt *c* permeabilizes CL-containing membranes. GUV confocal microscopy images. (A) DOPC with NBD-PE (left vesicle) and 80:20 DOPC:CL (right vesicle), treated with Alexa Fluor 568–cyt *c* in solution (red). (B) The 80:20 DOPC:CL GUV with NBD-PE, treated with fluorescent 70-kDa dextran (green) and Alexa Fluor 633–cyt *c* in solution (red). (C–E) Time series of 80:20 DOPC:CL GUVs with NBD-PE, treated with fluorescent 10-kDa dextran (green) and Alexa Fluor 633–cyt *c* in solution (red). In all images, the cyan lipid dye is 0.5 mol% NBD-PE. Average normalized cyt *c* and dextran concentration for each vesicle interior vs. background is plotted.

events uncomplicated by the addition of cyt *c* solution. The observed lag time due to this experimental setup may in part correspond to that observed in similar experiments with the pore-forming protein equinotoxin II (25).

We analyzed 165 GUVs from these confocal movies. The exterior and interior brightness of cyt *c* and dextran in each vesicle over time were extracted and plotted (Fig. S2). From these extracted leakage plots, along with close visual inspection of the movies, a spectrum of vesicle behaviors emerged as follows: “full leak”: vesicle leaks to at least ~80% of background in cyt *c* and dextran channels; “partial leak”: vesicle leaks and then plateaus at less than ~80% of background in cyt *c* and dextran channels; “leak stop leak”: vesicle leaks and then plateaus as described for the partial leak behavior; a second leakage event is then observed after the plateau; “no leak”: vesicle is not observed to leak to cyt *c* or dextran within the 45-min movie; “leaky to cyt *c* only”: vesicle leaks to cyt *c* (interior concentration of cyt *c* increases), but not to dextran (interior concentration of dextran remains low); and “complicated leakage”: vesicle behavior is complicated by vesicle collapse, contraction, or aggregation, as we have previously reported (29).

Fig. 2 shows representative plots for GUVs treated with cyt *c*. An abrupt change of the interior plot from zero or minimal slope to a steep slope indicates the instant when leakage begins; this observation is interpreted as the opening of a lipid pore, corresponding to an all-or-none type of leakage described in literature (27). Behavior and event timing varied for GUVs within a single sample, implying that pore formation is a stochastic process, whereas initial binding of cyt *c* to the membrane was fast. The fact that both cyt *c* and dextran plots followed the same trajectory indicates that both leaked simultaneously in nearly every GUV (Fig. 2A). Fig. 2B illustrates representative behaviors of GUVs; the partial leak plot shows that pores can close before equilibrium is reached across the membrane, and the leak-stop-leak plot suggests that after the closing of one pore, another pore may open. Permeability values of GUV membranes were calculated from the normalized dextran leakage data (Fig. 2C and D).

This experiment was repeated with nonfluorescent horse heart cyt *c* and dextran. Vesicle leakage was monitored by dextran brightness over time, because the nonfluorescent cyt *c* could not be observed. Twelve GUVs treated with horse heart cyt *c* were analyzed; behavior types and permeability values were essentially identical to vesicles treated with yeast cyt *c* (Fig. 2D).

Leakage movies were taken of GUVs with a variety of compositions: 10–20 mol% CL, with or without 25 mol% cholesterol, and with or without phase separation (29). All of these GUVs showed similar pore formation behaviors and similar permeability values (Fig. 2D did not contain composition distinctions). By contrast, membranes lacking CL were not observed to leak when treated with cyt *c*, demonstrating that the presence of CL is necessary and sufficient for the formation of pores by cyt *c*.

Our studies also suggested that cholesterol plays a supporting role in pore formation, although GUVs both with and without cholesterol were observed to leak. Because of the relatively small number of vesicles observed in microscope studies, we used a complementary technique to confirm the role of cholesterol. A leakage assay using carboxyfluorescein-encapsulated large unilamellar vesicles (LUVs) yielded quantitative ensemble measurements on large numbers of vesicles; a fluorescence increase was associated with LUV leakage or destruction. The results showed that CL-containing LUVs treated with horse heart or yeast cyt *c* exhibited leakage above that seen in control 1-palmitoyl-2-oleoyl-*sn*-glycero-3-phosphocholine (POPC) LUVs, and that leakage was exacerbated when 10 mol% cholesterol was also present (Fig. S4, SI Text). Leakage was dramatically reduced in the presence of ATP (Fig. S5, SI Text).

## Discussion

The interactions of cyt *c* with phospholipid membranes are clearly very complex, involving electrostatic and hydrophobic interactions (5, 30, 31), demixing of the lipid components (23), changes in lipid curvature (6, 22), and conformational changes in the protein (1, 9–11). Single-GUV microscopy has the advantage of allowing the direct observation of individual vesicles with different lipid compositions side by side. The GUVs in these

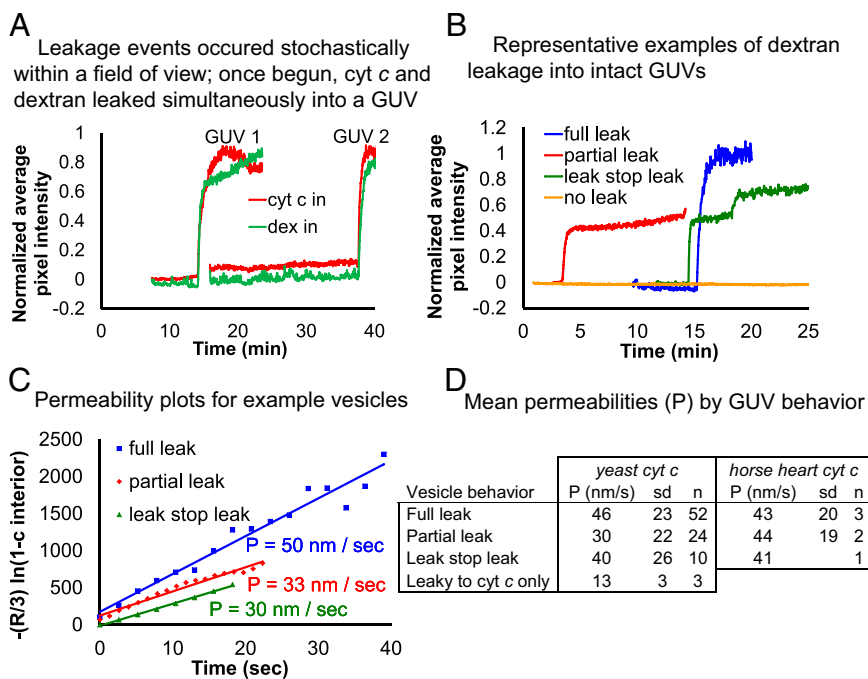


**Fig. 2.** Leakage of *cyt c* and dextran into vesicles is simultaneous and can proceed with intact vesicles. (A) Normalized average pixel intensity data in *cyt c* (red) and 10-kDa dextran (green) channels for the interior of two representative GUVs within one sample. (B) Interior dextran normalized average pixel intensity data for behavior-representative vesicles. (C) Permeability plot for example vesicles:  $-(R/3) \ln(1 - c_{\text{interior}})$  is plotted vs. time; permeability is best-fit line slope. (D) Table of permeability values (in nanometers per second) sorted by behavior (sd is SD,  $n$  is number vesicles observed in the sample). Vesicle compositions: (A and B) leak stop leak 25:40:10:25 DOPC:DPPC:CL:chol (phase-separated); (B) full 65:10:25 DOPC:CL:chol; (B) partial 80:20 DOPC:CL; (B) no leak 27.5:37.5:10:25 DOPC:DPPC:CL:chol (phase-separated). All vesicles contain 0.5 mol% NBD-PE; phase-separated also contain 0.5 mol% Rh-PE. All vesicles are pretreated with dextran and monitored after *cyt c* addition.

experiments did not exchange their lipids to any observable degree, as is demonstrated by the lipid dye remaining over time in one population of vesicles in a mixed sample. This observation of multiple GUV populations under the same conditions showed that *cyt c* binds strongly only to CL-containing membranes (Fig. 1A). A very weak fluorescent halo is seen in the red channel around the DOPC GUV in Fig. 1A, which might be attributable to a very weak association of *cyt c* with the membrane, or to a low level of bleed-through signal from the lipid dye (blue) channel.

Following the recruitment of *cyt c* to the outer leaflet by CL, the CL-*cyt c* conjugate caused membrane leakage, and a rapid flux of *cyt c* into the GUV interior occurring over a period of 1–2 min (Figs. 1C–E and 2A). Several lines of evidence lead to the conclusion that the leakage is caused by the opening of size-limited pores. The leak time profiles showed “bursts” of *cyt c* influx, with GUV interiors rapidly coming to equilibrium (Fig. 2A). This observation is consistent with the opening of a stable membrane pore—corresponding with an all-or-none type of leakage (27)—rather than the translocation of individual *cyt c* molecules across the membrane in separate locations, which has previously been envisioned as a sort of “burrowing” through the membrane in inverted micelle-like structures (6). The time course of dextran influx followed the same trajectory as that of *cyt c* (Fig. 2A), further demonstrating the existence of stable pores, which remained open to all molecules below a certain cutoff size; the larger 70-kDa dextran was excluded from GUV interiors (Fig. 1B). Finally, some GUVs exhibited a partial leak behavior (Fig. 2B) where leakage began and then abruptly stopped before reaching equilibrium, an observation consistent with the closing of a single membrane pore in that GUV and indicating the overall reversibility of the pore-forming process. This observation also indicates that pore formation under these conditions is a rare event, because a large number of *cyt c* molecules has been recruited to the membrane surface. Added ATP significantly decreased the rate and extent of vesicle leakage, suggesting an aspect of competitive inhibition and possibly a feedback system that diminishes *cyt c*-CL interactions at high ATP concentrations.

Permeability is the property of a membrane that quantifies the rate of translocation of specific molecules and is independent of

their concentration difference across the membrane and the GUV size. For a GUV of 10- $\mu\text{m}$  diameter, with 0  $\mu\text{M}$  *cyt c* in its interior volume and 5  $\mu\text{M}$  *cyt c* in its external environment, a permeability value of 40 nm/s (Fig. 2D) corresponds to an initial net flow of  $\sim 4 \times 10^4$  *cyt c* molecules entering the GUV per second through the open pore. This net flux will decrease exponentially as the interior concentration tends to an equilibrium concentration equal to that of *cyt c* in the external environment. At this point, *cyt c* will continue to translocate the membrane; however, the influx and efflux of *cyt c* will be equal such that no net change in the GUV’s interior concentration is observed.

The membrane permeability was examined for the leaking GUVs (Fig. 2C and D), and the pore size was estimated from the permeability values, by comparing results to those obtained for equinatoxin II, a member of the family of 20-kDa pore-forming toxins from sea anemones (25). Permeability was also determined by a calculation of diffusive transport. These two approaches yielded pore diameters of  $\sim 2$  and  $\sim 20$  nm, respectively, reasonably comparable to the diameter of *cyt c* ( $\sim 3$  nm). (See *SI Text* for calculations and discussion.) These pore size values are also comparable to the estimated diameter of the inverted hexagonal channels described in earlier work,  $\sim 2$ –3 nm (6). There was no difference in the behavior or permeability of GUVs treated with yeast *cyt c* vs. horse heart *cyt c*.

We reported previously that single-GUV microscopy on a similar system revealed another fascinating morphological change induced in membranes by *cyt c*—the dramatic collapse of CL-containing liquid-disordered domains in phase-separated vesicles (29). In this work, we excluded the permeability values of GUVs that appeared to undergo any type of collapse, contraction, or aggregation during or before leakage, as any leakage in these vesicles could have been caused by destructive processes rather than pore formation. The permeability values for GUVs with “complicated leakage” behaviors were higher and far more variable than the permeability values for GUVs with apparently uncomplicated leakage, attributable to pore formation.

The pore-forming process observed here may be related to the ability of *cyt c* to induce a negative curvature stress upon binding to CL-containing membranes (6, 22, 23). The initial steps of this interaction could occur by local demixing and clustering of CL

through electrostatic attractions and by decreasing the preferred spontaneous curvature for the clustered lipid molecules and neutralizing the repulsive electrostatic interaction between CL head groups (Fig. 3B).

The negative curvature stress induced by cyt *c* would decrease the energetic barrier for the transition from a bilayer membrane (Fig. 3A) to a different lipid phase with a negative curvature, with head groups more closely spaced than lipid tails. The inverted hexagonal ( $H_{II}$ ) phase is one such structure that has been observed in experiments on CL-containing membranes treated with cyt *c* (6, 23); another structure with a barrier of formation significantly decreased by an increase in negative spontaneous curvature is a small-diameter toroidal lipid pore (Fig. 3B and C). The toroidal pore contains both negative (in the plane of the membrane) and positive (normal to the membrane

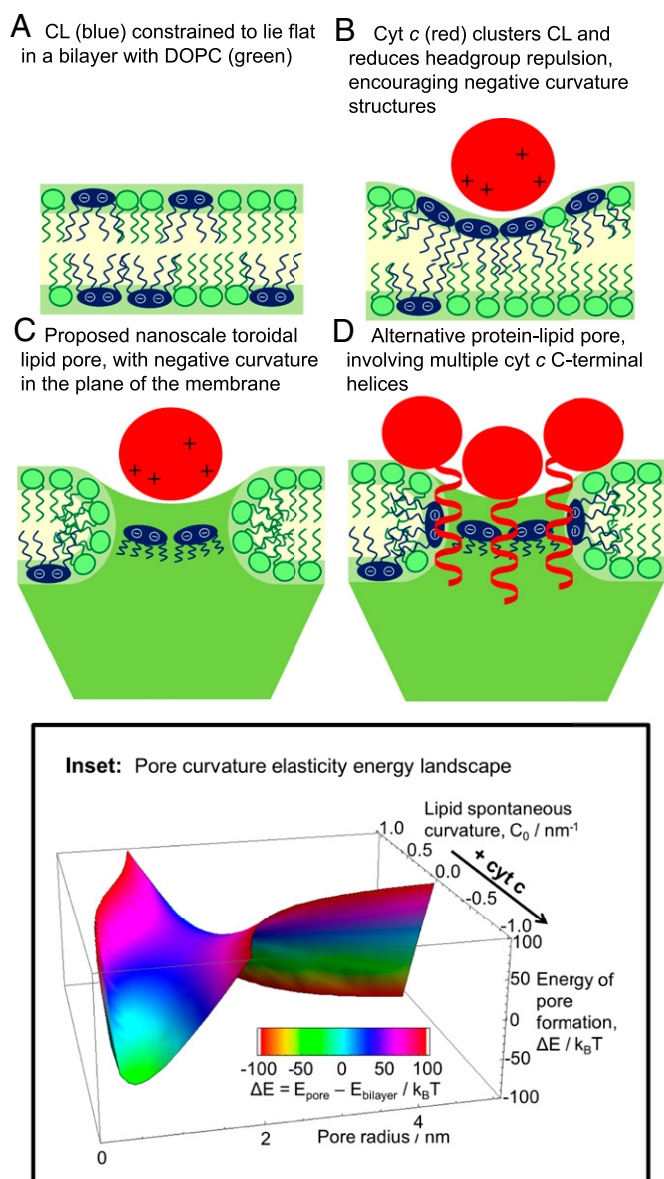


**Fig. 3.** Proposed cyt *c*-induced nanoscale toroidal lipid pore formation. (A–C) Cyt *c* induces formation of a toroidal pore of nanoscale radius, clustering negative-curvature lipid CL along the pore perimeter in the membrane plane. (D) Pore lined with a cluster of cyt *c* C-terminal helices. (Inset) Pore curvature elasticity energy landscape shows feasibility of pore formation with increasingly negative lipid spontaneous curvature.

plane) curvature; the balance of these is determined by the relative sizes of the pore diameter and the bilayer thickness (Fig. S6) (22). Therefore, we examined the difference in curvature elastic energy for lipid monolayers between a planar bilayer (Fig. 3A) and a toroidal lipid pore (Fig. 3B and C) of the same surface area. The curvature elastic energy of a fluid, elastic membrane can be calculated using the Helfrich model (32) as follows:  $e = \frac{\kappa_b}{2}(C_1 + C_2 - 2C_0)^2 + \kappa_G C_1 C_2$ , where  $e$  is the curvature elastic energy per unit area,  $C_1$  and  $C_2$  are the principal monolayer curvatures,  $C_0$  is the lipid monolayer's spontaneous (preferred) curvature, the bending modulus,  $\kappa_b$ , is taken to be  $5 k_B T$  for an unsaturated lipid monolayer (33), and the Gaussian curvature modulus,  $\kappa_G$ , is taken as  $\kappa_G = -0.8\kappa_b$ , within the permitted physical range  $-1 \leq \kappa_G / \kappa_b \leq 0$  (34).

The curvature elasticity energy landscape for varying pore radius and monolayer spontaneous curvature is shown in Fig. 3 Inset and Fig. S7. It should be noted that Gaussian curvature term provides a fixed energetic penalty for the topology change from a planar bilayer to the formation of a pore that is independent of the pore size. Therefore, a shift in the chosen value of  $\kappa_G$  only translates the energy landscape up or down the energy axis without transforming the shape of this surface. A deep energy minimum appears in the lower left corner for decreasing spontaneous curvature, predicting a metastable, finite-size pore with a thermally accessible energy difference from the planar bilayer state. This model predicts this metastable pore to be  $\sim 2$  nm in diameter, consistent with the above estimates from permeability. For the full calculation and discussion, see *SI Text*.

We find no evidence that the size (or curvature) of the GUV impacts pore formation. This is unsurprising because GUV curvatures are of the order of micrometer $^{-1}$ , which is effectively flat on macromolecular length scales (35). We observe leakage in both LUVs, radii of  $\sim 50$ – $100$  nm, and GUVs, radii of  $\sim 3$ – $20$   $\mu\text{m}$  (the radii of mitochondria are  $\sim 250$ – $500$  nm). Therefore, vesicle size does not affect the process, except that a larger vesicle will provide a greater surface area over which pore formation can occur; this is consistent with the slower population-wide leakage observed in LUV vs. GUV experiments.

Some cationic proteins and peptides do induce toroidal pores via negative curvature stress, as our model suggests for cyt *c* (Fig. S8); these species include HIV-transactivator of transcription (TAT), tachyplesin, islet amyloid polypeptide, 14-helical  $\beta$ -peptides, NK-2 (a cationic core peptide from natural killer lysin, or NK-lysin), and sticholysins I and II (36–43). Lysozyme—a protein of similar size, shape, and charge to cyt *c*—caused similar leakage to cyt *c* in our LUV experiments (Fig. S4). Interestingly, several studies suggest that truncated BH3 interacting-domain death agonist (tBid) and/or Bcl-2-associated X protein (BAX) may cause outer mitochondrial membrane lipidic pores related to curvature (18–21). Other species that cause membrane structural changes in analogous ways include modified lipids and cationic nanoparticles (44, 45).

This exacerbation of leakage from cholesterol-containing membranes (Fig. S4) seems counterintuitive at first glance because cholesterol generally decreases membrane permeability by increasing lipid packing density (46). Indeed, in this work, cholesterol did protect membranes from leakage in the absence of CL (Fig. S4). However, membranes containing cholesterol have a significant negative spontaneous curvature; in this system, the effect may be synergistic with the effect of cyt *c* on CL in lowering the barrier for pore formation. Cholesterol has also been found to promote pore formation by *Vibrio cholerae* cytotoxin (47).

The effects of cholesterol and ATP on the interaction of cyt *c* with CL are suggestive of a role for this pore formation activity in apoptosis. Cholesterol is found mainly in the outer mitochondrial membrane, whereas CL is present in the inner membrane under nonapoptotic conditions. The apoptotic migration of CL

to the outer membrane—which contains high levels of cholesterol—may create a membrane permeable enough for cyt *c* to act upon. Similarly, emerging research suggests that the abundant ATP present in the mitochondria may bind to cyt *c*, altering the conformation and activities of the protein (15, 48); mitochondrial ATP levels may therefore regulate whether cyt *c* acts as an electron transporter or a proapoptotic protein.

As is clear from the time dependence of cyt *c* binding and subsequent membrane permeation (Fig. 1 *C–E* and Fig. S3), the initial association of the protein to the outer leaflet of CL-containing vesicles was fast, whereas leakage occurred only after minutes. We suggest that the slow phase of pore formation may involve conformational changes that occur after the initial protein–lipid binding. These changes include CL acyl tail insertion into the hydrophobic cleft of cyt *c*—in accord with the extended anchor model of cyt *c* CL–membrane interaction (30, 31, 49)—and the recently described equilibration between compact and extended lipid-bound cyt *c* conformations (1, 12). One such scenario is depicted in Fig. 3*D*. Here, the C-terminal helix, which begins after the distal heme ligand, Met-80, and contains the conserved Arg-91, has unfolded to stabilize the open pore. Worrall and coworkers (5) have recently shown that Arg-91 has a significant effect on the CL-induced redox activity of cyt *c*, and Pletneva and coworkers (1, 12) have shown with time-resolved FRET measurements that CL interactions with cyt *c* cause a portion of the protein to exist in an extended conformation with an unfolded C-terminal helix. Moreover, this C-terminal peptide is membrane permeable (24). Inspection of the amino acid sequence of this C-terminal helical region of cyt *c* reveals a highly conserved –KKEERAD– sequence beginning with Lys-88. Helical wheel analysis shows a cluster of positive charges along one helix face, including Arg-91, and a polar surface with a cluster of negative charges on the opposite face. This arrangement would allow both electrostatic CL interactions with the positive helix surface to stabilize the pore and a polar and carboxylate-rich pore lining to facilitate passage of cyt *c*, not complexed with CL, as is observed (Fig. 3*D*).

In summary, we find that cyt *c* and CL in synthetic membranes can recreate some of the events required for membrane permeation and release of cyt *c*. The phenomena occur at lower concentrations than are estimated to exist in mitochondrial intermembrane space [estimates range as high as 5 mM (50)] and in the absence of other apoptotic machinery. The apoptotic migration of CL to the cholesterol-containing outer membrane (7) may attract cyt *c* to the outer membrane and afford cyt *c* the opportunity to act—either independently of, or possibly in cooperation with, other permeabilizing apoptotic agents such as tBid and Bax—on the outer membrane and help engineer its own escape. Other aspects of the cyt *c*–ATP–CL interaction in lipid vesicles are under current study.

## Materials and Methods

**Materials and Protein Labeling.** DOPC, 1,2-dipalmitoyl-*sn*-glycero-3-phosphocholine (DPPC), POPC, CL (heart, bovine-disodium salt), and cholesterol (chol) were purchased from Avanti Polar Lipids. *N*-(7-nitrobenz-2-oxa-1,3-diazol-4-yl)-1,2-dihexadecanoyl-*sn*-glycero-3-phosphoethanolamine, triethylammonium salt (NBD-PE); Lissamine rhodamine B 1,2-dihexadecanoyl-*sn*-glycero-3-phosphoethanolamine, triethylammonium salt (Rh-PE); Alexa Fluor 568 C<sub>5</sub> maleimide; Alexa Fluor 633 C<sub>5</sub> maleimide; and fluorescent dextran molecules (Texas Red-dextran conjugate, neutral, 10,000 and 70,000 molecular weight) were purchased from Invitrogen. Horse heart cyt *c*, yeast (*Saccharomyces cerevisiae*) cyt *c* (isoform 1), chicken egg white lysozyme, and all other reagents were purchased from Sigma-Aldrich. Yeast cyt *c* was labeled with maleimide dyes as described in the literature (29, 51, 52).

**GUV Formation.** GUVs were formed by electroformation. Stock solutions of 1.0 mM total lipid in chloroform were made. Twenty to 50  $\mu$ L of stock solution was placed dropwise onto the platinum wires of the electroformation chamber and dried under vacuum for 4 h. The chamber was then filled with 300 mM aqueous sucrose solution, and a 3.0-V alternating current (or 1.0-V

alternating current for mixtures containing anionic lipids) electric field was applied across the wires at 10 Hz for 30 min, 3.0 Hz for 15 min, 1.0 Hz for 7 min, and 0.5 Hz for 7 min. For samples containing lipids with melting temperatures above room temperature, electroformation was conducted in an oven at temperatures of at least 50 °C; vesicles were then allowed to slowly cool to room temperature. GUVs composed entirely of lipids with melting temperatures below ambient conditions were formed by this protocol at room temperature.

**Confocal Microscopy.** Vesicle samples were imaged at room temperature using the Leica TCS SP5 confocal system with Leica 63 $\times$ /1.3 N.A. Plan Apo differential interference contrast glycerin immersion lens. Rh-PE, Alexa Fluor 568, and Texas Red were excited by diode-pumped solid-state laser at 561 nm; Texas Red was additionally excited by helium–neon laser at 594 nm; NBD-PE (a head group-labeled lipid with similar spectral properties to FITC) was excited by argon laser at 488 nm; and Alexa Fluor 633 was excited by helium–neon laser at 633 nm.

Glass bottom culture dishes were pretreated with 10% (vol/vol) BSA solution to prevent vesicles from adhering to glass, rinsed with deionized water, and dried. Twenty-five to 50  $\mu$ L of prepared vesicle suspension and 50  $\mu$ L of microscope buffer (10 mM Hepes, pH 7.4, adjusted to 336 mOsm with NaCl) were deposited on the glass slide and incubated ~15 min to allow vesicles to settle to a single focal plane at the bottom of the sample.

Cyt *c* was dialyzed against microscope buffer. Dextran solutions were prepared in microscope buffer. A stock solution of cyt *c* or dextran (3–10  $\mu$ M final diluted concentration) was added carefully to the top of the sample drop. Control experiments were performed with DOPC vesicles to obtain a zero-leakage measurement.

Cyt *c* was slightly in excess in the experiments. The cyt *c*:CL ratio varied from ~2:1 to ~40:1. In addition, the amount of cyt *c* in a sample was greater than what would fit on both leaflet surfaces of the GUVs. With a radius of ~1.5 nm, cyt *c* occupies a surface area of ~700  $\text{\AA}^2$ , whereas CL and DOPC occupy areas of ~120 and ~70  $\text{\AA}^2$ , respectively. For a GUV composed of 80:20 DOPC:CL, an average lipid molecule, then, would have a surface area of ~80  $\text{\AA}^2$ , and cyt *c* would saturate the surface of a GUV at a ratio of ~1:9 cyt *c*:total lipid, or ~1:2 cyt *c*:CL. This excess allowed us to observe the movement of non-lipid-bound cyt *c* from the GUV exterior to the interior.

**Analysis of Confocal Images and Movies.** Confocal images and movies were analyzed using Leica Application Suite Advanced Fluorescence software. Vesicles that appeared multilamellar, aggregated before leaking, or had a diameter of less than 8  $\mu$ m were not analyzed. Some vesicles that did not leak during the movies were analyzed for comparison. Vesicles were monitored over time for average fluorescent pixel intensity (correlating with concentration) for both dextran and cyt *c* fluorophores in a region of interest (ROI) that was manually centered in the interior of the vesicle cross section. This ROI was moved as needed to keep it within the vesicle interior. Monitoring was discontinued if the vesicle aggregated, collapsed, moved out of the field of view, or moved away from the monitoring ROI after leakage. Background intensity was monitored by placing an ROI near but outside the vesicle.

Concentration ( $c_{\text{interior},t}$ ) was normalized on a scale of 0–1 according to the equation  $c_{\text{interior},t} = (b_{\text{interior},t} - b_{\text{interior,control}}) / (b_{\text{exterior}} - b_{\text{interior,control}})$ , with  $b$  representing average pixel intensity and  $b_{\text{interior,control}}$  representing in images average interior pixel intensity for the nonleaking DOPC control experiment, and in movies the average interior pixel intensity at time 0. For normalized leakage plots,  $b_{\text{exterior}}$  was defined as the maximum average pixel intensity in an exterior ROI in any frame during monitoring of the leakage; to calculate permeability,  $b_{\text{exterior}}$  was defined as the average pixel intensity in an exterior ROI at time  $t$ . Vesicle permeability ( $P$ ) was taken as the gradient of the log-linear plot of the leakage profile plotted, in a manner similar to refs. 25 and 26, as  $-R/3 \ln(1 - c_{\text{interior},t})$  against time  $t$ , with  $R$  as the GUV radius; derivation is from Nelson (53). Using Adobe Photoshop, images were enhanced only for brightness, contrast, color balance, and color levels.

**Preparation of Carboxyfluorescein-Encapsulated Large Unilamellar Vesicles.** Lipid thin films were deposited by evaporating chloroform lipid solutions (10  $\mu$ mol of total lipid per sample) in test tubes under argon and then overnight vacuum. The 100 mM 5-(and-6)-carboxyfluorescein was dissolved in LUV buffer (100 mM Hepes, pH 7.4, buffer with 150 mM NaCl). One milliliter of carboxyfluorescein solution was added to the tubes. Samples were incubated 30 min at 40 °C and then sonicated for 30 min via probe-tip sonicator in an ice-water bath. Suspensions were centrifuged 5 min at 10,000  $\times$  *g* relative centrifugal force and pipetted off sonicator tip debris. Samples were

subjected to five freeze–thaw cycles using liquid nitrogen and a 40 °C water bath and extruded at 40 °C 19 times through a 200-nm pore size polycarbonate membrane using an Avanti Mini-Extruder. Vesicles were separated from nonencapsulated carboxyfluorescein using Sephadex G-25 PD-10 columns.

**Carboxyfluorescein Leakage Assays.** Protein stock solutions were prepared in LUV buffer and run over DEAE Sephadex. Assays were performed on a Varian fluorescence microplate reader from Thermo Electron Corporation. Samples were excited at 470 nm and monitored at 525 nm (bandwidth, 12 nm). After initial fluorescence measurements, 100- $\mu$ L aliquots of carboxyfluorescein-encapsulated LUVs were treated with stock solutions or LUV buffer for control (final diluted concentrations: 60  $\mu$ M lysozyme or horse

heart cyt c, 30  $\mu$ M yeast cyt c, 0.1% Triton X-100). Fluorescence measurements were taken every 5 min. Samples treated with Triton X-100 were used to determine maximum fluorescence ( $f_{max}$ ). Results at time  $x$  ( $f_x$ ) were normalized on a scale of 0–100 by subtracting the background signal at time 0 ( $f_0$ ) according to the equation:  $f_{normalized} = (f_x - f_0)/(f_{max} - f_0) \times 100$ . Carboxyfluorescein leakage in the presence of ATP was carried out similarly with added ATP at 2.75–16.7 mM final concentration (Fig. S5).

**ACKNOWLEDGMENTS.** We thank Dr. Jia Su for discussions, Dr. John Eng for support on mass spectroscopy, and Dr. Joseph Goodhouse for assistance with the confocal microscope and software. We acknowledge the National Institutes of Health for support of this work (Method to Extend Research in Time Award 2R37 GM036298 to J.T.G.) and fellowship support from Eli Lilly (C.L.B.).

- Hong Y, Muenzner J, Grimm SK, Pletneva EV (2012) Origin of the conformational heterogeneity of cardiolipin-bound cytochrome c. *J Am Chem Soc* 134(45):18713–18723.
- Ow YP, Green DR, Hao Z, Mak TW (2008) Cytochrome c: Functions beyond respiration. *Nat Rev Mol Cell Biol* 9(7):532–542.
- Lahiri J, Fate GD, Ungashe SB, Groves JT (1996) Multi-heme self-assembly in phospholipid vesicles. *J Am Chem Soc* 118(10):2347–2358.
- Abe M, Niibayashi R, Koubori S, Moriyama I, Miyoshi H (2011) Molecular mechanisms for the induction of peroxidase activity of the cytochrome c-cardiolipin complex. *Biochemistry* 50(39):8383–8391.
- Rajagopal BS, Silkstone GG, Nicholls P, Wilson MT, Worrall JAR (2012) An investigation into a cardiolipin acyl chain insertion site in cytochrome c. *Biochim Biophys Acta* 1817(5):780–791.
- de Kruijff B, Cullis PR (1980) Cytochrome c specifically induces non-bilayer structures in cardiolipin-containing model membranes. *Biochim Biophys Acta* 602(3):477–490.
- Ardail D, et al. (1990) Mitochondrial contact sites. Lipid composition and dynamics. *J Biol Chem* 265(31):18797–18802.
- Schug ZT, Gottlieb E (2009) Cardiolipin acts as a mitochondrial signalling platform to launch apoptosis. *Biochim Biophys Acta* 1788(10):2022–2031.
- Kagan VE, et al. (2005) Cytochrome c acts as a cardiolipin oxygenase required for release of proapoptotic factors. *Nat Chem Biol* 1(4):223–232.
- Balakrishnan G, et al. (2007) A conformational switch to beta-sheet structure in cytochrome c leads to heme exposure. Implications for cardiolipin peroxidation and apoptosis. *J Am Chem Soc* 129(3):504–505.
- Su J, Groves JT (2010) Mechanisms of peroxy-nitrite interactions with heme proteins. *Inorg Chem* 49(14):6317–6329.
- Hanske J, et al. (2012) Conformational properties of cardiolipin-bound cytochrome c. *Proc Natl Acad Sci USA* 109(1):125–130.
- Hüttemann M, et al. (2011) The multiple functions of cytochrome c and their regulation in life and death decisions of the mammalian cell: From respiration to apoptosis. *Mitochondrion* 11(3):369–381.
- Pecina P, et al. (2010) Phosphomimetic substitution of cytochrome C tyrosine 48 decreases respiration and binding to cardiolipin and abolishes ability to trigger downstream caspase activation. *Biochemistry* 49(31):6705–6714.
- Sinibaldi F, et al. (2008) Insights into cytochrome c-cardiolipin interaction. Role played by ionic strength. *Biochemistry* 47(26):6928–6935.
- Landeta O, et al. (2011) Reconstitution of proapoptotic BAK function in liposomes reveals a dual role for mitochondrial lipids in the BAK-driven membrane permeabilization process. *J Biol Chem* 286(10):8213–8230.
- Schäfer B, et al. (2009) Mitochondrial outer membrane proteins assist Bid in Bax-mediated lipidic pore formation. *Mol Biol Cell* 20(8):2276–2285.
- Epand RF, Martinou JC, Fornalaz-Mulhauser M, Hughes DW, Epand RM (2002) The apoptotic protein tBid promotes leakage by altering membrane curvature. *J Biol Chem* 277(36):32632–32639.
- Kuwana T, et al. (2002) Bid, Bax, and lipids cooperate to form supramolecular openings in the outer mitochondrial membrane. *Cell* 111(3):331–342.
- Terrones O, et al. (2004) Lipidic pore formation by the concerted action of proapoptotic BAX and tBid. *J Biol Chem* 279(29):30081–30091.
- Basañez G, et al. (2002) Bax-type apoptotic proteins porate pure lipid bilayers through a mechanism sensitive to intrinsic monolayer curvature. *J Biol Chem* 277(51):49360–49365.
- Seddon JM (1990) Structure of the inverted hexagonal (HII) phase, and non-lamellar phase transitions of lipids. *Biochim Biophys Acta* 1031(1):1–69.
- Trusova VM, Gorbenko GP, Molotkovsky JG, Kinnunen PKJ (2010) Cytochrome c-lipid interactions: New insights from resonance energy transfer. *Biophys J* 99(6):1754–1763.
- Jones S, Holm T, Mäger I, Langel U, Howl J (2010) Characterization of bioactive cell penetrating peptides from human cytochrome c: Protein mimicry and the development of a novel apoptogenic agent. *Chem Biol* 17(7):735–744.
- Schön P, et al. (2008) Equinotoxin II permeabilizing activity depends on the presence of sphingomyelin and lipid phase coexistence. *Biophys J* 95(2):691–698.
- Fuertes G, et al. (2010) Pores formed by Bax $\alpha$ 5 relax to a smaller size and keep at equilibrium. *Biophys J* 99(9):2917–2925.
- Apellániz B, Nieva JL, Schwille P, Garcia-Sáez AJ (2010) All-or-none versus graded: Single-vesicle analysis reveals lipid composition effects on membrane permeabilization. *Biophys J* 99(11):3619–3628.
- Alam JM, Kobayashi T, Yamazaki M (2012) The single-giant unilamellar vesicle method reveals lysenin-induced pore formation in lipid membranes containing sphingomyelin. *Biochemistry* 51(25):5160–5172.
- Beales PA, Bergstrom CL, Geerts N, Groves JT, Vanderlick TK (2011) Single vesicle observations of the cardiolipin-cytochrome C interaction: Induction of membrane morphology changes. *Langmuir* 27(10):6107–6115.
- Kalanxhi E, Wallace CJA (2007) Cytochrome c impaled: Investigation of the extended lipid anchorage of a soluble protein to mitochondrial membrane models. *Biochem J* 407(2):179–187.
- Tuominen EK, Wallace CJ, Kinnunen PK (2002) Phospholipid-cytochrome c interaction: Evidence for the extended lipid anchorage. *J Biol Chem* 277(11):8822–8826.
- Helfrich W (1973) Elastic properties of lipid bilayers—theory and possible experiments. *Z Naturforsch C* 28(11):693–703.
- Marsh D (2006) Elastic curvature constants of lipid monolayers and bilayers. *Chem Phys Lipids* 144(2):146–159.
- Templer RH, Khoo BJ, Seddon JM (1998) Gaussian curvature modulus of an amphiphilic monolayer. *Langmuir* 14(26):7427–7434.
- Domanov YA, et al. (2011) Mobility in geometrically confined membranes. *Proc Natl Acad Sci USA* 108(31):12605–12610.
- Mishra A, Gordon VD, Yang L, Coridan R, Wong GCL (2008) HIV TAT forms pores in membranes by inducing saddle-splay curvature: Potential role of bidentate hydrogen bonding. *Angew Chem Int Ed Engl* 47(16):2986–2989.
- Imura Y, Nishida M, Ogawa Y, Takakura Y, Matsuzaki K (2007) Action mechanism of tachyplesin I and effects of PEGylation. *Biochim Biophys Acta* 1768(5):1160–1169.
- Doherty T, Waring AJ, Hong M (2006) Peptide-lipid interactions of the beta-hairpin antimicrobial peptide tachyplesin and its linear derivatives from solid-state NMR. *Biochim Biophys Acta* 1758(9):1285–1291.
- Smith PES, Brender JR, Ramamoorthy A (2009) Induction of negative curvature as a mechanism of cell toxicity by amyloidogenic peptides: The case of islet amyloid polypeptide. *J Am Chem Soc* 131(12):4470–4478.
- Epand RF, Raguse TL, Gellman SH, Epand RM (2004) Antimicrobial 14-helical beta-peptides: Potent bilayer disrupting agents. *Biochemistry* 43(29):9527–9535.
- Jacobs T, Bruhn H, Gaworski I, Fleischer B, Leippe M (2003) NK-lysin and its shortened analog NK-2 exhibit potent activities against *Trypanosoma cruzi*. *Antimicrob Agents Chemother* 47(2):607–613.
- Willumeit R, et al. (2005) Structural rearrangement of model membranes by the peptide antibiotic NK-2. *Biochim Biophys Acta* 1669(2):125–134.
- Valcarcel CA, et al. (2001) Effects of lipid composition on membrane permeabilization by sticholysin I and II, two cytolytins of the sea anemone *Stichodactyla helianthus*. *Biophys J* 80(6):2761–2774.
- Zidovska A, et al. (2009) Block liposomes from curvature-stabilizing lipids: Connected nanotubes, -rods, or -spheres. *Langmuir* 25(5):2979–2985.
- Zhang ZY, Smith BD (2000) High-generation polycationic dendrimers are unusually effective at disrupting anionic vesicles: Membrane bending model. *Bioconjug Chem* 11(6):805–814.
- Ohvo-Rekilä H, Ramstedt B, Leppimäki P, Slotte JP (2002) Cholesterol interactions with phospholipids in membranes. *Prog Lipid Res* 41(1):66–97.
- Krasilnikov OV, et al. (2007) Pore formation by *Vibrio cholerae* cytotoxin requires cholesterol in both monolayers of the target membrane. *Biochimie* 89(3):271–277.
- Patriarca A, et al. (2009) ATP acts as a regulatory effector in modulating structural transitions of cytochrome c: Implications for apoptotic activity. *Biochemistry* 48(15):3279–3287.
- Kapetanaki SM, et al. (2009) Interaction of carbon monoxide with the apoptosis-inducing cytochrome c-cardiolipin complex. *Biochemistry* 48(7):1613–1619.
- Forman HJ, Azzi A (1997) On the virtual existence of superoxide anions in mitochondria: Thoughts regarding its role in pathophysiology. *FASEB J* 11(5):374–375.
- Perroud TD, Bokoch MP, Zare RN (2005) Cytochrome c conformations resolved by the photon counting histogram: Watching the alkaline transition with single-molecule sensitivity. *Proc Natl Acad Sci USA* 102(49):17570–17575.
- Lee AJ, Ensign AA, Krauss TD, Bren KL (2010) Zinc porphyrin as a donor for FRET in Zn(II)cytochrome c. *J Am Chem Soc* 132(6):1752–1753.
- Nelson P (2004) *Biological Physics: Energy, Information, Life* (Freeman, New York).

# Supporting Information

Bergstrom et al. 10.1073/pnas.1303819110

## SI Additional Microscopy Results

A control experiment (Fig. S1) shows that, before the addition of cytochrome *c* (cyt *c*), 10-kDa dextran is excluded from the interior of giant unilamellar vesicles (GUVs). The average pixel intensity inside GUVs remains essentially at zero even after several hours of incubation with 10-kDa dextran, demonstrating that it is the presence of cyt *c* that causes these vesicles to leak to the dextran.

The pixel brightness in the interior of a GUV can be monitored over time, in histogram format for each frame, as in Fig. S2. The GUV interior brightness histogram starts at 0 min at the same level as a dark (unleaked) control vesicle and over 3.5 min increases, converging to the brightness of the exterior space.

During the microscopy movies of leakage, cyt *c* and dextran background concentrations were monitored by average pixel intensity in an exterior region of interest (ROI) (Fig. S3). These data were used to normalize interior pixel intensities, as described in *Materials and Methods*.

## SI Large Unilamellar Vesicle Carboxyfluorescein Leakage Assay Results

The results show that cardiolipin (CL)-containing membranes treated with horse heart cyt *c*, yeast cyt *c*, or lysozyme show leakage above that seen in control 1-palmitoyl-2-oleoyl-*sn*-glycero-3-phosphocholine (POPC) vesicles; leakage is enhanced when 10% cholesterol is also present in the membranes (Fig. S4).

Large unilamellar vesicles (LUVs) (20% cardiolipin, 10% cholesterol, 70% POPC) encapsulated with 100 mM carboxyfluorescein were made by the extrusion method, and then run through PD-10 size exclusion column to remove excess carboxyfluorescein. After infusion of the LUV with horse heart cyt *c* (64  $\mu$ M final concentration), carboxyfluorescein efflux out of the LUV was measured by the fluorescence increase. The relative fluorescence intensity was calculated and plotted vs. time. The addition of ATP reduced the rate and extent of relative fluorescence intensity in a concentration-dependent manner (Fig. S5).

## SI Curvature Elastic Energy Difference Between a Flat Bilayer and a Bilayer Containing a Toroidal Lipid Pore

The curvature elastic energy,  $E$ , of a lipid monolayer of area  $A$ , modeled as a homogeneous elastic sheet, is given by Eq. S1 as follows:

$$E = \frac{\kappa_b}{2} \int (C_1 + C_2 - 2C_0)^2 dA + \kappa_G \int C_1 C_2 dA, \quad [\text{S1}]$$

where  $C_1$  and  $C_2$  are the principal curvatures of the membrane in orthogonal, in-plane directions, and  $C_i = 1/r_i$ , where  $r_i$  is the radius of curvature of the principal curvatures,  $C_i$ . It is conventional to define monolayer curvatures that bend toward the aqueous phase as negative and monolayer curvatures that bend away from the aqueous phase as positive. The spontaneous curvature,  $C_0$ , is the preferred curvature of the monolayer in its relaxed, unstressed state. The two bending moduli,  $\kappa_b$  and  $\kappa_G$ , are the bending energy modulus and Gaussian bending modulus of the lipid monolayer. We take  $\kappa_b = 5k_B T$  for a lipid monolayer with unsaturated acyl chains (2). Values for  $\kappa_G$  are much harder to measure experimentally, but theory constrains the Gaussian curvature modulus of a lipid monolayer to be in the range  $-1 \leq \kappa_G/\kappa_b \leq 0$  (3), and the few experimental studies that have been conducted find values of around  $\kappa_G = -0.8\kappa_b$  (3, 4), which is the value we initially take in our calculations.

We calculate the monolayer curvature elastic energy difference,  $\Delta E$ , between a flat lipid bilayer with total monolayer area  $A^*$  and the same total area of lipid monolayer with a toroidal lipid pore of area  $A_{\text{pore}}$  and flat bilayer of area  $(A^* - A_{\text{pore}})$ . Therefore,

$$\Delta E = E_{\text{pore}} + e_{\text{bilayer}}(A^* - A_{\text{pore}}) - e_{\text{bilayer}}A^* = E_{\text{pore}} - e_{\text{bilayer}}A_{\text{pore}}, \quad [\text{S2}]$$

where  $e_{\text{bilayer}}$  is the curvature elastic energy per unit area of the lipid monolayers of a flat lipid bilayer. Because for a flat bilayer  $C_1 = C_2 = 0$ , then

$$e_{\text{bilayer}} = 2\kappa_b C_0^2. \quad [\text{S3}]$$

The monolayer area of a toroidal lipid pore,  $A_{\text{pore}}$ , of internal radius  $R_2$  and monolayer thickness  $R_1$  can be calculated in cylindrical polar coordinates, denoting  $R' = R_1 + R_2$ , (Fig. S6) as follows:

$$A_{\text{pore}} = \int dA = \int_0^{2\pi} \int_{-R_1}^{R_1} \rho dz d\phi, \quad [\text{S4}]$$

$$A_{\text{pore}} = \int_0^{2\pi} d\phi \int_{-R_1}^{R_1} R' - \sqrt{R_1^2 - z^2} dz, \quad [\text{S5}]$$

$$A_{\text{pore}} = 2\pi \left( [R'z]_{-R_1}^{R_1} - \int_{-R_1}^{R_1} \sqrt{R_1^2 - z^2} dz \right). \quad [\text{S6}]$$

Substituting  $z = R_1 \sin \theta$ , such that  $dz = R_1 \cos \theta d\theta$  and  $\theta = \arcsin(z/R_1)$ . Thus, the limits of the integral become  $-\pi/2 \leq \theta \leq \pi/2$ . Then,

$$A_{\text{pore}} = 2\pi \left( 2R'R_1 - \int_{-\pi/2}^{\pi/2} \left\{ \sqrt{R_1^2(1 - \sin^2 \theta)} \right\} R_1 \cos \theta d\theta \right), \quad [\text{S7}]$$

$$A_{\text{pore}} = 2\pi \left( 2R'R_1 - \int_{-\pi/2}^{\pi/2} R_1^2 \cos^2 \theta d\theta \right), \quad [\text{S8}]$$

$$A_{\text{pore}} = 4\pi R'R_1 - 2\pi R_1^2 \left[ \frac{1}{2} (\theta - \sin \theta \cos \theta) \right]_{-\pi/2}^{\pi/2}, \quad [\text{S9}]$$

$$A_{\text{pore}} = 4\pi R'R_1 - \pi^2 R_1^2 = 4\pi(R_1 + R_2)R_1 - \pi^2 R_1^2. \quad [\text{S10}]$$

To calculate  $E_{\text{pore}}$ , we must first define the two principal curvatures of the toroidal pore,  $r_1$  and  $r_2$ . From Fig. S5, we can deduce that  $r_1 = R_1$  is constant over the whole surface of the pore. Therefore,

$$C_1 = \frac{1}{R_1}. \quad [\text{S11}]$$

We use Fig. S6 to define  $r_2$ , finding  $\tan \varphi = z/\sqrt{R_1^2 - z^2}$  and  $\cos \varphi = (R' - \sqrt{R_1^2 - z^2})/r_2$ . Using the trigonometric identity,

$\cos \varphi = 1/\sqrt{1 + \tan^2 \varphi}$  and realizing that  $C_2$  is negative inside the toroidal pore, simple algebra reveals that

$$C_2 = -\frac{\sqrt{R_1^2 - z^2}}{R_1 \left( R' - \sqrt{R_1^2 - z^2} \right)}. \quad [\text{S12}]$$

First, we will solve the Gaussian curvature elasticity term of Eq. **S1** as follows:

$$\begin{aligned} \kappa_G \int C_1 C_2 dA &= \kappa_G \int_0^{2\pi} d\phi \int_{-R_1}^{R_1} \frac{-\sqrt{R_1^2 - z^2}}{R_1^2 \left( R' - \sqrt{R_1^2 - z^2} \right)} \left( R' - \sqrt{R_1^2 - z^2} \right) dz \\ &= -\frac{2\pi\kappa_G}{R_1^2} \int_{-R_1}^{R_1} \sqrt{R_1^2 - z^2} dz = -\pi^2 \kappa_G. \end{aligned} \quad [\text{S13}]$$

The last step is solved by the same method of substitution as used in calculating  $A_{\text{pore}}$ . Therefore, the Gaussian curvature contribution to the formation of a toroidal lipid pore is independent of the size of the pore, i.e., independent of both  $R_1$  and  $R_2$ . This invariance in Gaussian curvature for variations of the same topology is consistent with the requirements of the Gauss–Bonnet Theorem. The Gaussian curvature term in the curvature elasticity equation only contributes to the change in energy for changes in membrane topology where stretching or tearing of the elastic sheet is required for rearrangement into the new shape configuration. Changes in shape for the same topology only require bending of the elastic membrane, and hence only the first term in Eq. **S1** contributes to the change in energy. It should also be noted here that, although this contribution to the curvature elastic energy is negative,  $\kappa_G$  is required to be negative for a lipid monolayer, and hence this term provides a positive contribution to the change in curvature energy for the formation of a toroidal pore and hence necessitates an energy cost from this term for creation of the saddle-splay curvature inside this lipid pore.

Second, we examine the first term on the right-hand side of Eq. **S1**, the curvature elastic energy difference caused by monolayer bending as follows:

where

$$\begin{aligned} I_1 &= \int_{-R_1}^{R_1} \left( \frac{(1 - 2C_0 R_1)^2 \left( R' - \sqrt{R_1^2 - z^2} \right)^2}{\left( R' - \sqrt{R_1^2 - z^2} \right)} \right) dz \\ &= (1 - 2C_0 R_1)^2 \int_{-R_1}^{R_1} \left( R' - \sqrt{R_1^2 - z^2} \right) dz, \end{aligned} \quad [\text{S15}]$$

$$I_2 = \int_{-R_1}^{R_1} \left( \frac{(R_1^2 - z^2)}{\left( R' - \sqrt{R_1^2 - z^2} \right)} \right) dz, \quad [\text{S16}]$$

$$\begin{aligned} I_3 &= \int_{-R_1}^{R_1} \left( \frac{-2(1 - 2C_0 R_1) \left( R' - \sqrt{R_1^2 - z^2} \right) \sqrt{R_1^2 - z^2}}{\left( R' - \sqrt{R_1^2 - z^2} \right)} \right) dz \\ &= -2(1 - 2C_0 R_1) \int_{-R_1}^{R_1} \sqrt{R_1^2 - z^2} dz. \end{aligned} \quad [\text{S17}]$$

Integrals  $I_1$  and  $I_3$  can be solved similarly to the integral for our earlier calculation of  $A_{\text{pore}}$ . So that, for  $I_1$ ,

$$I_1 = (1 - 2C_0 R_1)^2 \left\{ 2R_1 R' - \frac{\pi R_1^2}{2} \right\}, \quad [\text{S18}]$$

and, for  $I_3$ ,

$$I_3 = -2(1 - 2C_0 R_1) \left\{ \frac{\pi R_1^2}{2} \right\} = -\pi R_1^2 (1 - 2C_0 R_1). \quad [\text{S19}]$$

The integral  $I_2$  cannot be solved analytically and is instead solved numerically using the Mathematica software package.

Therefore, substituting  $I_1$ ,  $I_2$ , and  $I_3$  back into Eq. **S14**, and then substituting this term for the bending energy along with Eq. **S13**, the Gaussian bending energy, back into Eq. **S1** and

$$\begin{aligned} \frac{\kappa_b}{2} \int (C_1 + C_2 - 2C_0)^2 dA &= \frac{\kappa_b}{2} \int_0^{2\pi} d\phi \int_{-R_1}^{R_1} \left( \frac{1}{R_1} - \frac{\sqrt{R_1^2 - z^2}}{R_1 \left( R' - \sqrt{R_1^2 - z^2} \right)} - 2C_0 \right)^2 \left( R' - \sqrt{R_1^2 - z^2} \right) dz \\ &= \pi \kappa_b \int_{-R_1}^{R_1} \left( \frac{R' - \sqrt{R_1^2 - z^2} - \sqrt{R_1^2 - z^2} - 2C_0 R_1 \left( R' - \sqrt{R_1^2 - z^2} \right)}{R_1 \left( R' - \sqrt{R_1^2 - z^2} \right)} \right)^2 \left( R' - \sqrt{R_1^2 - z^2} \right) dz \\ &= \frac{\pi \kappa_b}{R_1^2} \int_{-R_1}^{R_1} \left( \frac{(1 - 2C_0 R_1)^2 \left( R' - \sqrt{R_1^2 - z^2} \right)^2 + (R_1^2 - z^2) - 2(1 - 2C_0 R_1) \left( R' - \sqrt{R_1^2 - z^2} \right) \sqrt{R_1^2 - z^2}}{\left( R' - \sqrt{R_1^2 - z^2} \right)} \right) dz \\ &= \frac{\pi \kappa_b}{R_1^2} \{ I_1 + I_2 + I_3 \}, \end{aligned} \quad [\text{S14}]$$

rearranging, we find that the curvature elastic energy of a toroidal lipid pore is as follows:

$$E_{\text{pore}} = \pi\kappa_b(1 - 2C_0R_1) \left[ (1 - 2C_0R_1) \left( \frac{2(R_1 + R_2)}{R_1} - \frac{\pi}{2} \right) - \pi \right] + \frac{\pi\kappa_b}{R_1^2} \int_{-R_1}^{R_1} \frac{(R_1^2 - z^2)}{(R' - \sqrt{R_1^2 - z^2})} dz - \pi^2\kappa_G. \quad [\text{S20}]$$

Next, combining Eq. S3 and Eq. S10, we find that the curvature elastic energy of a flat bilayer of equivalent surface area is as follows:

$$E_{\text{bilayer}} = 2\pi R_1\kappa_b C_0^2(4(R_1 + R_2) - \pi R_1). \quad [\text{S21}]$$

Therefore, we can now examine the curvature elastic energy landscape for the difference between a toroidal lipid pore and a flat bilayer,  $\Delta E = E_{\text{pore}} - E_{\text{bilayer}}$ , with varying pore radius  $R_2$  and local monolayer spontaneous curvature,  $C_0$ .

Setting the thickness of the lipid bilayer ( $2R_1$ ) to be 5 nm, the curvature elasticity energy landscape for toroidal lipid pore formation in a flat bilayer is shown in Fig. 3B of the main manuscript. Below, in Fig. S7A, we show plots of  $\Delta E$  vs. pore radius ( $R_2$ ) for varying spontaneous curvatures,  $C_0$ . This demonstrates how the model predicts that, for decreasing local spontaneous curvature, the energy difference between a finite size nanoscale pore and a flat bilayer decreases. Note that, for macromolecules that might induce a positive local spontaneous curvature in a lipid bilayer, the model predicts pores that would continually grow without reaching a stable energy minimum for a finite sized pore.

In Fig. S7B, we examine the effects of changes in local Gaussian curvature modulus on the energy difference between a toroidal pore and a flat bilayer at a constant  $C_0$  ( $= -0.33 \text{ nm}^{-1}$ ) over the permissible range  $-1 \leq \kappa_G/\kappa_b \leq 0$ . We have taken  $\kappa_G = -0.8\kappa_b$  in our previous calculations. However, the Gaussian curvature modulus can be calculated as the second moment of the lateral pressure profile of the lipid monolayer (2, 3, 5–7) as follows:

$$\kappa_G = - \int_0^\ell P(z)(z - \xi)^2 dz, \quad [\text{S22}]$$

where  $P(z)$  is the lateral pressure profile,  $z$  is the depth in the monolayer of thickness  $\ell$ , and  $\xi$  is the pivotal surface (the depth of the monolayer that maintains constant area upon monolayer bending deformations). A qualitative model of the lateral pressure profile in a lipid monolayer (3, 6, 8) is shown in Fig. S8. Therefore, changes in the local interlipid interactions induced by cyt  $c$  binding to the membrane could also play a role in modulating the energy difference between the flat bilayer and toroidal pore states. We propose two ways in which cyt  $c$  might be expected to tune the lateral stresses between lipids. First, neutralization of the anionic CL head groups by the polycationic cyt  $c$  would reduce electrostatic repulsion between lipids in the head group region of the monolayer. Second, the acyl chain that inserts into cyt  $c$  (9, 10), anchoring the protein to the membrane, reduces the number of lipid chains in the hydrophobic region of the monolayer and thereby reduces the lateral steric repulsion between lipids in the acyl chain region. Both of these mechanisms reduce lateral repulsion between lipids and thereby would result in an increase in the monolayer  $\kappa_G$ . Fig S7B demonstrates that our model predicts such an increase in  $\kappa_G$  would decrease the energy difference between a pore and a flat bilayer, thereby

augmenting the favorability of a lipid pore that is already created by local clustering of negative spontaneous curvature lipids.

The curvature elasticity energy landscape demonstrates that a deep energy minimum appears for decreasing spontaneous curvature, predicting a metastable, finite-size nanopore. For example, taking  $\kappa_G = -0.8\kappa_b$ , a membrane with local spontaneous curvature  $C_0 = -0.5 \text{ nm}^{-1}$  has a local energy minimum that predicts a pore of diameter 1.4 nm with an energy difference of  $\Delta E = 18 k_B T$  from the bilayer state (Fig. S7A). Although this predicted pore size is slightly smaller than the size of the protein (2- to 3-nm diameter), it is of the correct order of magnitude and is consistent with reported pore sizes for another pore-forming protein with a measured permeability nearly identical to that of cyt  $c$  (see next section).

The curvature energy of a pore does not need to be lower than that of a planar bilayer for pore formation to be likely. If we treat each individual cyt  $c$  bound to the GUV membrane as independent from one another, the Boltzmann equation of statistical physics can be used to predict the equilibrium probability of the membrane upon which each cyt  $c$  is bound being in the pore state compared with being in the planar bilayer state:  $n_p/(n_p + n_b) = 1/(1 + \exp[\Delta E/k_B T])$ , where  $n_i$  is the population of each state: pore ( $i = p$ ) or bilayer ( $i = b$ ). Therefore, in equilibrium, the probability of a membrane of local  $C_0 = -0.5 \text{ nm}^{-1}$  forming a toroidal lipid pore of radius 1.4 nm is  $n_p/(n_p + n_b) = 1.5 \times 10^{-8}$ . Taking a representative membrane coverage for cyt  $c$  bound to 20% CL vesicles of  $300 \text{ nmol}\cdot\text{m}^{-2}$  (11),  $5.7 \times 10^7$  cyt  $c$  molecules would be bound to the outer monolayer of a  $10\text{-}\mu\text{m}$  diameter GUV. Therefore, under these conditions and at equilibrium, the model predicts an average of 0.86 pores per  $10\text{-}\mu\text{m}$  diameter GUV. This would be consistent with our assumption that only a single pore per vesicle is usually responsible for our measured leakage profiles and our observation that leakage can stop abruptly by the closure of this pore. It should be noted that we do not know the exact value of local spontaneous curvature (or local Gaussian curvature modulus) induced by cyt  $c$  upon binding to the membrane and these numbers in the previous calculation are only taken as representative to demonstrate the statistical physics of pore formation despite the fact that the pore state is of higher energy than that of a planar bilayer.

### SI Estimation of Pore Size from Permeability

Interestingly, we note that when you weight similar GUV confocal leakage experiments for cyt  $c$  in this work and for the pore-forming protein equinatoxin II in the study by Schön et al. (12) by hydrodynamic radii, the permeability measurements are very similar. Our cyt  $c$ -induced permeability to 10-kDa dextran [2.4-nm Stokes radius (13)] was calculated to be  $\sim 40 \text{ nm/s}$ . In comparison, equinatoxin II caused GUV membrane permeability of  $\sim 140 \text{ nm/s}$  to Alexa Fluor 488, a small fluorophore [estimated Stokes radius around 0.68 nm, similar to the small fluorophore calcein (14)]. Because diffusion is inversely proportional to the radius of the diffusing agent, the average cyt  $c$ -induced permeability in these experiments would be  $\sim 140 \text{ nm/s}$ , if measured with the smaller dye, suggesting similar sizes for cyt  $c$ - and equinatoxin-induced pores. Equinatoxin II and the related sticholysins, which are suggested to form toroidal pores like cyt  $c$  (15, 16), have been estimated in other papers to cause the formation of pores of  $\sim 1\text{-nm}$  radius (17, 18), approximately consistent with our calculations in the section above for cyt  $c$ .

In addition to the treatment of membrane curvature above and in the body of the paper, we can estimate the pore size based upon the permeability measurements we have made for the GUVs. Assuming purely diffusive transport of the cyt  $c$  across the membrane, the permeability ( $P_m$ ) can be approximated by the following expression:

$$P_m = \frac{D_0}{\delta} \left( \frac{A_p}{A_v} \right), \quad [\text{S23}]$$

where  $D_0$  is the Stokes–Einstein diffusion coefficient of cyt  $c$  through a membrane pore,  $\delta$  is the membrane thickness (taken to be 5 nm),  $A_p$  is the area of the vesicle membrane taken up by pores, and  $A_v$  is the total surface area of the vesicle (19). Due to the stochastic nature of pore formation and the rapid filling of the vesicle once leakage begins, we assume that only a single pore is responsible for the increasing concentration profile inside the GUV. Therefore, approximating cyt  $c$  as a sphere of radius 1.5 nm, a permeability of 40 nm·s<sup>-1</sup> measured for a 10- $\mu$ m-diameter vesicle predicts a pore radius of  $\sim$ 11 nm. However, this simple model does not take into account interactions between cyt  $c$  and the membrane and between individual proteins. Therefore, we only assume this to be an order of magnitude estimate, demonstrating the formation of a nanoscale pore in the membrane.

The mismatch of the equinatoxin pore size and that calculated from curvature vs. the apparent pore radius from a simple diffusional model suggests that other transport processes (e.g., electrohydrodynamic interactions between the membrane and the proteins and chemical potential gradients across the membrane) are significant for the magnitude of the membrane permeability measured in our experiments.

### SI Materials and Methods: Equipment and Settings

Figure acquisition information is as follows: Fig. 1A:  $xy$  pixel dimensions, 116.6 nm; 512  $\times$  512 pixels; 8-bit resolution; lipid dye  $N$ -(7-nitrobenz-2-oxa-1,3-diazol-4-yl)-1,2-dihexadecanoyl-*sn*-glycero-3-phosphoethanolamine, triethylammonium salt (NBD-PE) [channel 1, excitation, 488 nm; laser power, 30%; laser acoustic optic tunable filter (AOTF), 12%; emission window, 496–558 nm]; cyt  $c$  dye Alexa Fluor 568 (channel 2, excitation, 561 nm; laser AOTF, 17%; emission window, 602–651 nm); Fig. 1B:  $xy$  pixel dimensions, 88 nm; 512  $\times$  512 pixels; 8-bit resolution; lipid dye NBD-PE (channel 1, excitation, 488 nm; laser power, 30%; laser AOTF, 21%; emission window, 496–558 nm), cyt  $c$  dye Alexa Fluor 633 (channel 1, excitation, 633 nm; laser AOTF, 17%; emission window, 650–743 nm), dextran dye Texas Red (channel

2, excitation, 561 and 594 nm; laser AOTF values, 16% and 17%, respectively; emission window, 602–642 nm); Fig. 1C:  $xy$  pixel dimensions, 126.7 nm; 512  $\times$  512 pixels; 8-bit resolution; lipid dye NBD-PE (channel 1, excitation, 488 nm; laser power, 30%; laser AOTF, 21%; emission window, 496–558 nm); cyt  $c$  dye Alexa Fluor 633 (channel 1, excitation, 633 nm; laser AOTF, 16%; emission window, 650–743 nm); dextran dye Texas Red (channel 2, excitation, 561 and 594 nm; laser AOTF values, 14% and 13%, respectively; emission window, 602–646 nm); Fig. 1D:  $xy$  pixel dimensions, 126.7 nm; 512  $\times$  512 pixels; 8-bit resolution; lipid dye NBD-PE (channel 1, excitation, 488 nm; laser power, 30%; laser AOTF, 29%; emission window, 496–558 nm), cyt  $c$  dye Alexa Fluor 633 (channel 1, excitation, 633 nm; laser AOTF, 16%; emission window, 650–743 nm), dextran dye Texas Red (channel 2, excitation, 561 and 594 nm; laser AOTF values, 15% and 16%, respectively; emission window, 602–646 nm); Fig. 1E:  $xy$  pixel dimensions, 126.7 nm; 512  $\times$  512 pixels; 8-bit resolution; lipid dye NBD-PE (channel 1, excitation, 488 nm; laser power, 30%; laser AOTF, 29%; emission window, 496–558 nm), cyt  $c$  dye Alexa Fluor 633 (channel 1, excitation, 633 nm; laser AOTF, 27%; emission window, 650–743 nm), dextran dye Texas Red (channel 2, excitation, 561 and 594 nm; laser AOTF values, 15% and 16% respectively; emission window, 602–646 nm); and Fig. S1:  $xy$  pixel dimensions, 88 nm; 512  $\times$  512 pixels; 8-bit resolution; lipid dye NBD-PE (channel 1, excitation, 488 nm; laser power, 30%; laser AOTF, 21%; emission window, 496–558 nm); cyt  $c$  dye Alexa Fluor 633 (channel 1, laser AOTF, 17%; excitation, 633 nm; emission window, 650–743 nm); dextran dye Texas Red (channel 2, excitation, 561 and 594 nm; laser AOTF values, 16% and 17%, respectively; emission window, 602–646 nm).

Pixel intensities used in calculating concentrations were taken from unenhanced images and movies using Leica Application Suite Advanced Fluorescence Software. The display lookup table in each channel in all images and movies is linear and covers the full range of the data. Images for publication were enhanced for brightness, contrast, color balance, and color levels using Adobe Photoshop. No processing was performed to enhance the resolution of any images.

1. Helfrich W (1973) Elastic properties of lipid bilayers—theory and possible experiments. *Z Naturforsch C* 28(11):693–703.
2. Marsh D (2006) Elastic curvature constants of lipid monolayers and bilayers. *Chem Phys Lipids* 144(2):146–159.
3. Templer RH, Khoo BJ, Seddon JM (1998) Gaussian curvature modulus of an amphiphilic monolayer. *Langmuir* 14(26):7427–7434.
4. Siegel DP, Kozlov MM (2004) The gaussian curvature elastic modulus of  $N$ -monomethylated dioleoylphosphatidylethanolamine: Relevance to membrane fusion and lipid phase behavior. *Biophys J* 87(1):366–374.
5. Kozlov MM, Leikin SL, Markin VS (1989) Elastic properties of interfaces—elasticity moduli and spontaneous geometric characteristics. *J Chem Soc Faraday Trans* 85(4): 277–292.
6. Marsh D (2007) Lateral pressure profile, spontaneous curvature frustration, and the incorporation and conformation of proteins in membranes. *Biophys J* 93(11): 3884–3899.
7. Marsh D (2008) Protein modulation of lipids, and vice-versa, in membranes. *Biochim Biophys Acta* 1778(7–8):1545–1575.
8. Marsh D (1996) Lateral pressure in membranes. *Biochim Biophys Acta* 1286(3): 183–223.
9. Kalanxhi E, Wallace CJA (2007) Cytochrome  $c$  impaled: Investigation of the extended lipid anchorage of a soluble protein to mitochondrial membrane models. *Biochem J* 407(2):179–187.
10. Tuominen EK, Wallace CJ, Kinnunen PK (2002) Phospholipid-cytochrome  $c$  interaction: Evidence for the extended lipid anchorage. *J Biol Chem* 277(11):8822–8826.
11. Salamon Z, Tollin G (1996) Surface plasmon resonance studies of complex formation between cytochrome  $c$  and bovine cytochrome  $c$  oxidase incorporated into a supported planar lipid bilayer. I. Binding of cytochrome  $c$  to cardiolipin/phosphatidylcholine membranes in the absence of oxidase. *Biophys J* 71(2):848–857.
12. Schön P, et al. (2008) Equinatoxin II permeabilizing activity depends on the presence of sphingomyelin and lipid phase coexistence. *Biophys J* 95(2):691–698.
13. Pearce RH, Grimmer BJ (1978) Calibration of agarose columns for gel chromatography with commercially available dextran fractions. Application to the measurement of distributions of molecular radii of glycosaminoglycans. *J Chromatogr A* 150(2): 548–553.
14. Kodama T, Hamblin MR, Doukas AG (2000) Cytoplasmic molecular delivery with shock waves: Importance of impulse. *Biophys J* 79(4):1821–1832.
15. Anderluh G, et al. (2003) Pore formation by equinatoxin II, a eukaryotic protein toxin, occurs by induction of nonlamellar lipid structures. *J Biol Chem* 278(46):45216–45223.
16. Valcarcel CA, et al. (2001) Effects of lipid composition on membrane permeabilization by sticholysin I and II, two cytolytins of the sea anemone *Stichodactyla helianthus*. *Biophys J* 80(6):2761–2774.
17. Tejuca M, Serra MD, Ferreras M, Lanio ME, Menestrina G (1996) Mechanism of membrane permeabilization by sticholysin I, a cytolytin isolated from the venom of the sea anemone *Stichodactyla helianthus*. *Biochemistry* 35(47):14947–14957.
18. Belmonte G, Pederzoli C, Macek P, Menestrina G (1993) Pore formation by the sea anemone cytolytin equinatoxin II in red blood cells and model lipid membranes. *J Membr Biol* 131(1):11–22.
19. Nelson P (2004) *Biological Physics: Energy, Information, Life* (Freeman, New York).

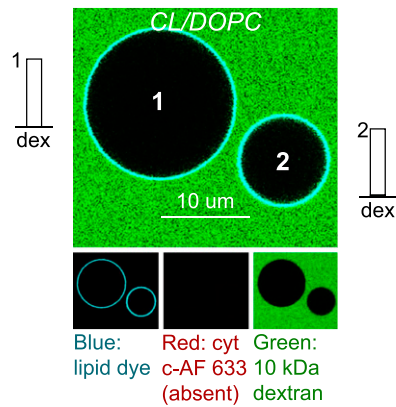


Fig. S1. In the absence of cyt c, GUVs treated with 10-kDa dextran do not leak.

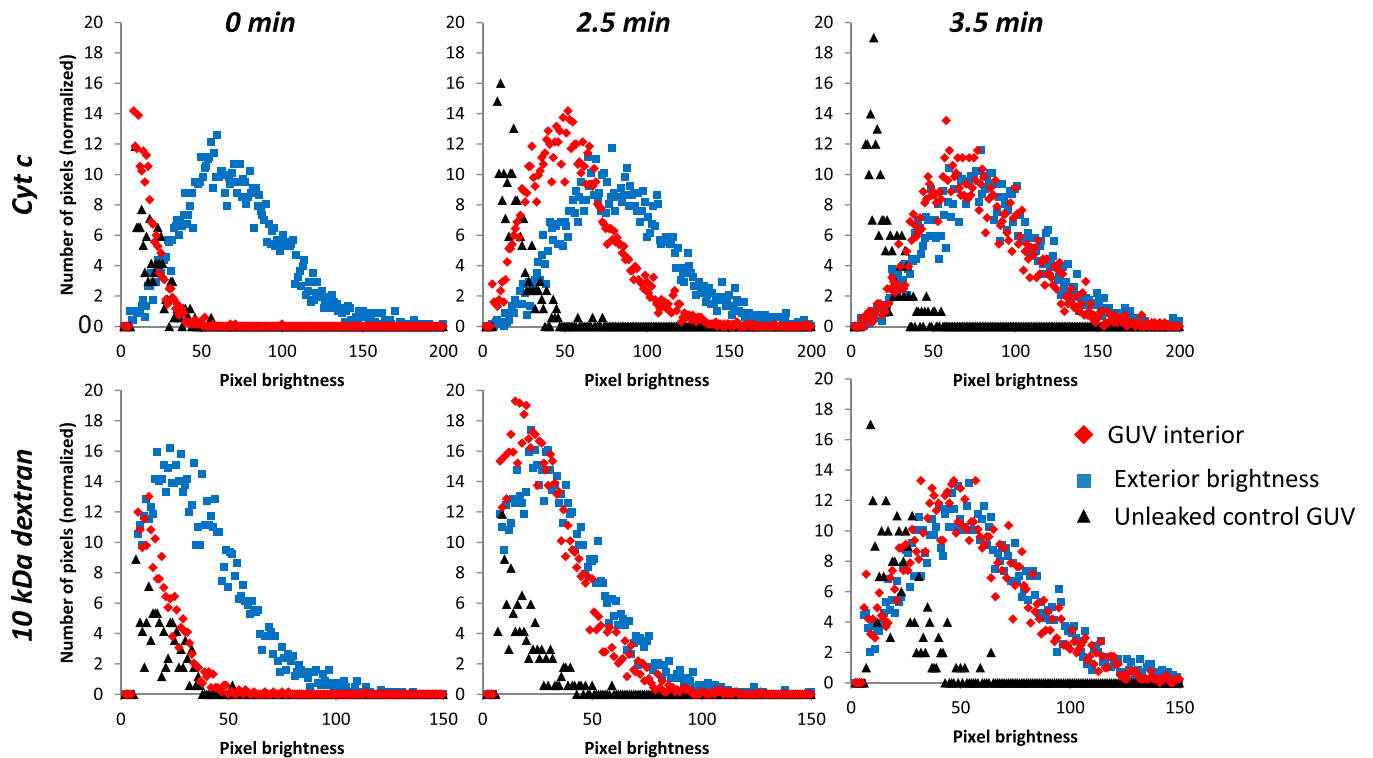


Fig. S2. GUV interior brightness approaches exterior brightness over time; this figure uses the same data as GUV 4 in Fig. 1 C–E in the main manuscript, with pixel brightness for cyt c and dextran channels plotted in histogram format. The data in this histogram are averaged for the bar graphs above GUV 4 in Fig. 1. The y axis here is normalized for ROI size.

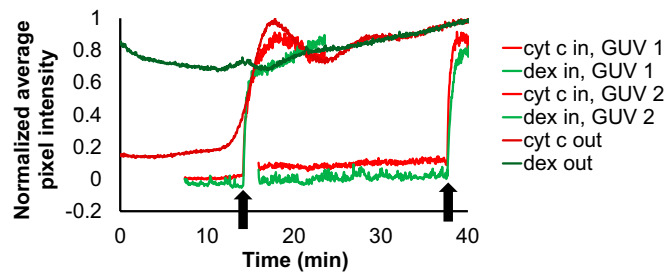


Fig. S3. The “arrival on the scene” of cyt c and background dextran intensity is monitored during microscopy movies of leakage; this figure uses the same data as Fig. 2A in the main manuscript, with additional traces to observe background intensities.

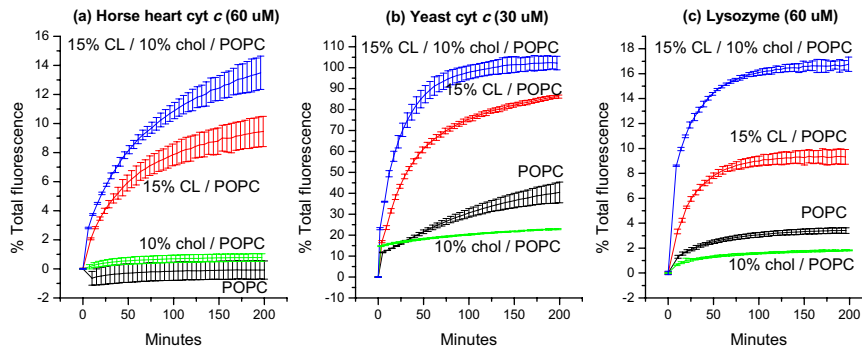


Fig. S4. Cholesterol enhanced cyt *c*-induced carboxyfluorescein leakage from CL-containing LUVs;  $n = 3$  measurements; error bars represent SD.

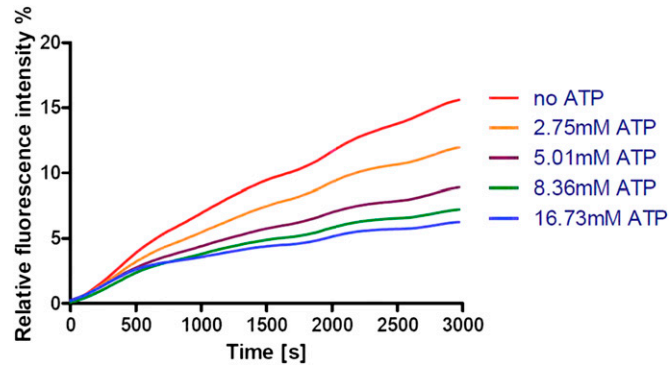


Fig. S5. Increasing ATP concentrations decreased cyt *c*-induced carboxyfluorescein leakage from CL-containing LUVs.

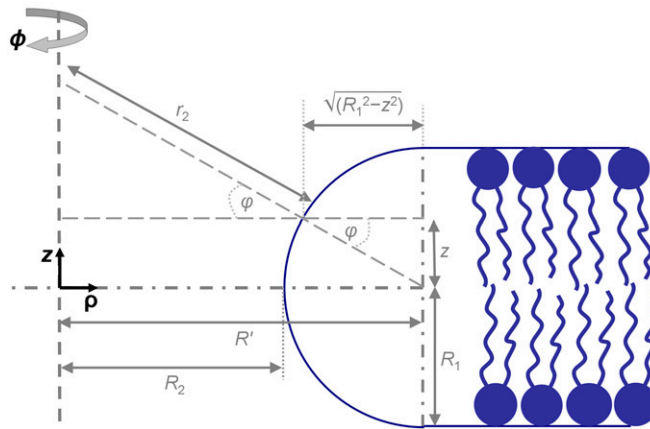


Fig. S6. Geometric calculations for a toroidal lipid pore in cylindrical polar coordinates.

